Temperature fluctuations and boundary layer turbulence as seen by Mars Exploration Rovers Miniature Thermal Emission Spectrometer

Emily L. Mason [a],[*], Michael D. Smith [b]

[a] NASA Postdoctoral Program Fellow, NASA Goddard Space Flight Center, 8800 Greenbelt Rd., Greenbelt, MD 20771, United States of America
[b] NASA Goddard Space Flight Center, 8800, Greenbelt Rd., Greenbelt, MD 20771, United States of America

ARTICLE INFO

ABSTRACT

The Mini-TES spectrometer carried by Spirit and Opportunity is a unique instrument that enabled vertical temperature profiles to be retrieved at high frequency (every 2 s, or "ICK"). Observations obtained from this instrument provide information on boundary layer activity. As an extension of previous work, we have retrieved ICK-by-ICK vertical temperature profiles to characterize turbulent behavior at each rover site for up to two Mars Years. We have also retrieved ICK-by-ICK near-surface (1.1 m) atmospheric temperatures and surface temperatures from dedicated atmospheric observations as well as geologic observations that extend the coverage of near-surface observations. The extension and increased frequency of retrievals as well as the additional observations provide a more complete view of the vertical and temporal variation of temperature fluctuations within the PBL. Temperature fluctuations are assessed using detrended temperature time-series data. The results show fluctuations can be as large as 10 K at the surface and 8 K aloft with timescales on the order of minutes. We have calculated the peak-to-peak amplitudes of temperature fluctuations and the corresponding timescales over which they occur. Spirit and Opportunity temperature fluctuation amplitudes decrease in magnitude vertically, where higher atmospheric levels show smaller fluctuations in amplitudes than at the surface. The magnitude of temperature fluctuations changes with the difference in surface and air temperature. This difference varies little as a function of season at both rover sites. Fluctuations are observed to quickly decrease in the late afternoon reaching a minimum near 17:00 LTST followed by moderately increased activity near sunset caused by forced convection. There is no significant change in the observed convective activity as a function of dust optical depth during regional dust storms. The few large temperature fluctuations that are concurrent with dust events are likely the result of large-scale systems.

1. Introduction

The Planetary Boundary Layer (PBL) is the layer of the atmosphere that interacts directly with the surface. It controls the transfer of heat, momentum, and mass to and from the free atmosphere and is strongly influenced by surface properties and solar heating. This is especially true on Mars, where the low atmospheric density enhances boundary layer processes (see Read et al., 2017 for a comprehensive review).

Spacecraft missions that operate from the Martian surface are capable of sampling the lowest portions of the PBL through measurements of pressure, wind, and temperature. Viking Landers 1 and 2 recorded winds, pressure, and temperature throughout the mission (Hess et al. 1977), and provided novel measurements that characterized boundary layer behavior (Sutton et al. 1978; Tillman et al. 1994).

Fluctuations in temperature data recorded with the Pathfinder Atmospheric Structure and Meteorology instrument (ASI/MET) showed nighttime mechanical forcing and strong daytime convective motions (Schofield et al. 1997). In addition to pressure at a single level, the Phoenix lander measured temperature with consistently high frequency at three levels on the lander mast (Taylor et al., 2008). It also measured winds using a telltale wind sensor at a frequency much less than that of temperature or pressure (Gunnlaugsson et al., 2008). Monin-Obukhov similarity theory parameters were derived and tested against this dataset (Davy et al., 2010) as they were for the Viking and Pathfinder landers (Larsen et al. 2002; Martínez et al. 2009).

Current in-situ data is available from both the Mars Science Laboratory (MSL) Curiosity rover (Grotzinger et al., 2012) and the InSight lander (Banerdt et al. 2020). For each sol, the Rover Environmental

Monitoring Station (REMS) onboard MSL records temperature and pressure every second at roughly 1.5 m above the surface for five minutes at the top of each hour (Gómez-Elvira et al., 2012). This cadence provides exceptional coverage for boundary layer studies (Miller et al. 2018), but due to complications with the wind sensors, wind data is no longer available (Newman et al. 2017). The Pressure Sensor (PS) and Temperature and Wind Sensors for InSight (TWINS) (Banfield et al. 2020) onboard the InSight lander measure meteorological variables at a higher frequency than that of REMS. The increased frequency and continuous measurements allow for improved analysis of boundary layer behavior compared to many previous missions. One thing that the Viking, Pathfinder, Phoenix, Curiosity and InSight missions have in common is that their in-situ temperature measurements are all confined to the lowest two meters of the atmosphere. Although these near-surface temperature observations have produced important results, they are not able to characterize PBL processes occurring above this height.

The Miniature Thermal Emission Spectrometer (Mini-TES) onboard the Mars Exploration Rovers (MER) Spirit and Opportunity measured thermal emission from the atmosphere and surface enabling the retrieval of near-surface atmospheric temperatures (Smith et al. 2006; Spanovich et al. 2006) and the vertical temperature profiles up to two kilometers (Smith et al., 2004, 2006). These profiles are available for almost two Mars Years (MY) from the beginning of each mission. The temperature profiles retrieved by Mini-TES are unique in their ability to provide insight into the vertical structure of short-timescale convective activity compared to other Mars surface missions.

Spirit (14.6°S, 175.5°E) landed in Gusev crater, a 160-km diameter Noachian-age impact crater on January 4, 2004 (MY 26, $L_s = 328°$), while Opportunity (1.9°S, 357.5°E) landed in Eagle crater on January 24, 2004 (MY 26, $L_s = 339°$), three weeks later (Squyres et al., 2003). Both rovers operated over the same time frame, allowing measurements of the PBL from two unique geographic locations at the same time.

Smith et al. (2006) and Spanovich et al. (2006) presented retrieval results using upward and downward-looking Mini-TES observations, respectively. The two types of observations were defined by their viewing geometry and consisted of sets of spectra recorded every two seconds at various local times throughout each sol. For the main results presented in both Smith et al., (2006) and Spanovich et al., (2006), the observed radiance spectra within a single observation were averaged together to retrieve temperature, dust optical depth and water vapor abundance in an iterative approach. Additionally, for a very limited number of observations, they discussed the variations in temperature when profiles were retrieved using individual spectra rather than averaged over an entire observation. This analysis showed that variations in the temperature signal could be as large as 8 K occurring over timescales of a minute or less. This work is an extension of the analysis of individually retrieved temperature profiles in order to characterize near-surface turbulence within the boundary layer on Mars.

A challenge for the characterization of the PBL using data from Spirit and Opportunity is that the rovers did not contain dedicated meteorological packages, making the retrievals from Mini-TES the only frequent measurement conducive to studying convective activity at those locations. 1-D model simulations of the vertical profiles from Mini-TES have been performed (Savijarvi et al., 2012a, 2012b; Sorbjan et al. 2009), but no full analysis of turbulence across each mission has been performed, and comparisons of convective activity between the two rovers have been limited.

Here we present work that utilizes temperature profile retrievals from individual Mini-TES spectra and extends the retrieval coverage to almost two MY for both downward and upward-looking observations. We use these high-frequency temperature retrievals to characterize boundary layer turbulence at the locations of Spirit and Opportunity rovers as a function of both season and local time. Section 2 reviews the retrieval algorithm. Section 3 presents retrieval results, including the seasonal and diurnal variations of short-timescale temperature fluctuations for Spirit and Opportunity. Finally, we discuss turbulence with respect to outside forcing such as dust and surface thermal inertia in section 4.

2. Data

The Mini-TES instrument was a Fourier transform spectrometer designed to obtain spectra between 339 and 1997 cm^{-1} (5 to 29 μm) at a spectral sampling of roughly 10 cm^{-1} (Christensen et al. 2003). Mini-TES instrument data have been used for both atmospheric (e.g., Smith et al. 2006; Spanovich et al. 2006) and geologic (e.g., Christensen et al. 2004a; Christensen et al. 2004b) investigations, which also provide information on near-surface atmospheric temperature. The acquisition time for each spectrum is two seconds, which is defined as one "ICK" (Integration Counter Keeper). Observations comprise sets of spectra numbering between 100 and 1275. Each acquired spectrum constitutes two seconds, so an observation can contain anywhere from about 3 to 42 min of continuous data. For the purposes of this paper, we define a "long stare" as an observation containing more than 900 spectra (approximately 30 min of data).

Individual Mini-TES observations are taken in either an upward or a downward-looking geometry. The former, which views the atmosphere, has been used to retrieve vertical temperature profiles from roughly 20 m to 2 km above the surface (Smith et al., 2004; Smith et al. 2006). The latter points towards the ground and provides information on near-surface atmospheric temperature and ground temperature (Spanovich et al. 2006; Smith et al. 2006). Upward-looking observations provide temperature profiles along a path determined by the line-of-sight. For example, atmospheric temperature at 2 km in altitude for an upward pointing observation at an elevation angle of 30° will provide information 4 km away. The near-surface temperature retrieved from the downward-looking geometry is representative of a height roughly 1.1 m above the surface (Spanovich et al. 2006; Smith et al. 2006).

Two types of upward-looking observations are available in the Mini-TES dataset. The first is an "elevation scan", which consecutively takes sets of 100 spectra at elevation angles 10°, 20° and 30° above the plane of the rover deck (which may or may not be the same as the plane of local level). The second is a "stare", which records spectra at a single elevation angle up to 42 min. The stare observations are used here to characterize turbulent behavior on scales of two seconds to half an hour (Smith et al. 2006).

Downward-looking observations were also obtained frequently throughout the mission for each rover (Spanovich et al. 2006). Within the CO_2 absorption band centered at 15 μm (667 cm^{-1}), the atmosphere between the sensor and the surface creates an absorption feature that is strong enough to allow the retrieval of temperatures for both the surface and the near-surface atmosphere 1.1 m above the surface within an area of 25 cm in diameter (Spanovich et al. 2006). The retrieval algorithm for these downward-looking observations is detailed in Spanovich et al. (2006), which includes results that cover the first 180 sols for Spirit and Opportunity. This work extends that of Spanovich et al. (2006) by presenting ICK-by-ICK results and extending the temporal coverage to all available observations for both rovers. Most downward-looking observations contain 5–10 spectra and last 10–20 s. A limited number of longer stares are available at single elevation angles that contain as many as 200 spectra (~8.5 min). These longer stares are included in the analysis to assess boundary layer temperatures on scales of seconds to minutes.

In our analysis we also include (downward-looking) geologic observations that are well-suited to provide near-surface atmospheric temperatures. These observations are processed using the same algorithm as the downward-looking observations that were intended specifically for determining near-surface atmospheric temperatures (Spanovich et al. 2006; Smith et al. 2006). The criterion for selection is that the observation has a single elevation angle pointed more than 10° below the plane of the rover deck for all ICKS within the observation. No raster scans are used.
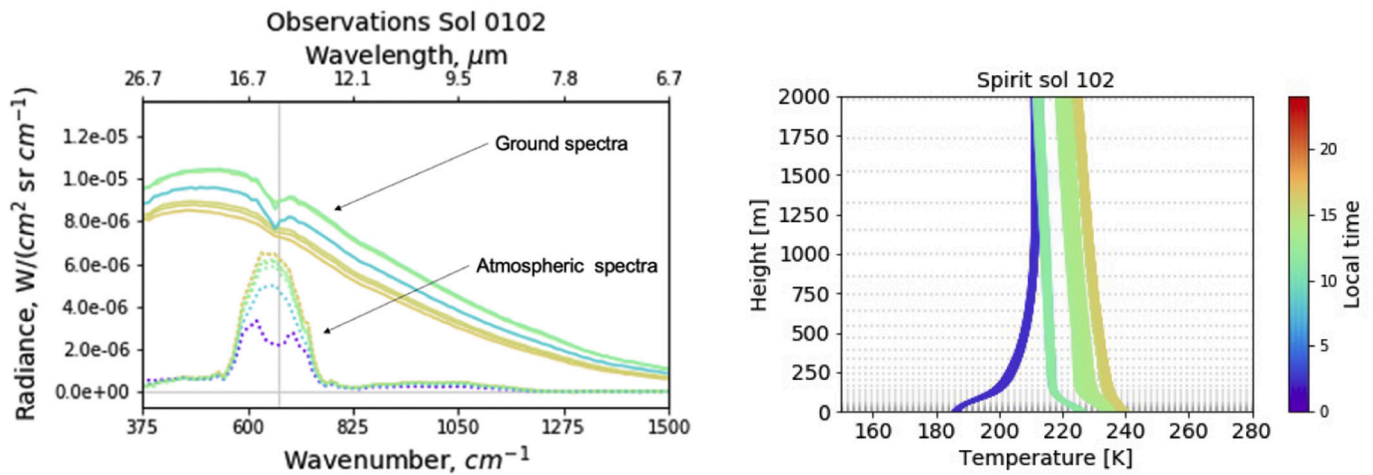
Fig. 1. (Left) Mini-TES radiances observed for downward and upward stares. Each spectrum shows a distinct emission/absorption feature from CO_2 gas for upward/downward observations. (Right) The resulting temperature retrievals on an ICK-by-ICK basis. All colors correspond to Local True Solar Time (LTST). Nighttime upward stares show an inversion layer, while daytime stares have a superadiabatic lapse rate near the surface.

2.1. Instrumentation and retrieval

The retrieval used in this work is the same as that described by Smith et al. (2006) and Spanovich et al. (2006), with the additional corrections described by Sorbjan et al. (2009). In this work, atmospheric temperatures are retrieved from an individual spectrum without averaging. Using a least-squares inversion, the vertical temperature profile is retrieved from upward-looking observations, or upward stares, within the CO_2 absorption band centered at 667 cm^{-1} (15 μm) (e.g. Smith et al.

2006). Gas absorptions observed in the spectra are modeled using the correlated-k approach (Lacis and Oinas 1991) with inclusion of a two-stream approximation to account for scattering from aerosols. The vertical coordinate used in the retrieval algorithm is logarithmic in pressure so that the vertical resolution increases near the surface and decreases at higher altitudes. Spectra and retrieval results are filtered with quality control criteria to remove data containing large systematic errors. This includes spectra with consistently non-physical values (e.g., below zero radiances) and retrieved temperatures that have unrealistic values.
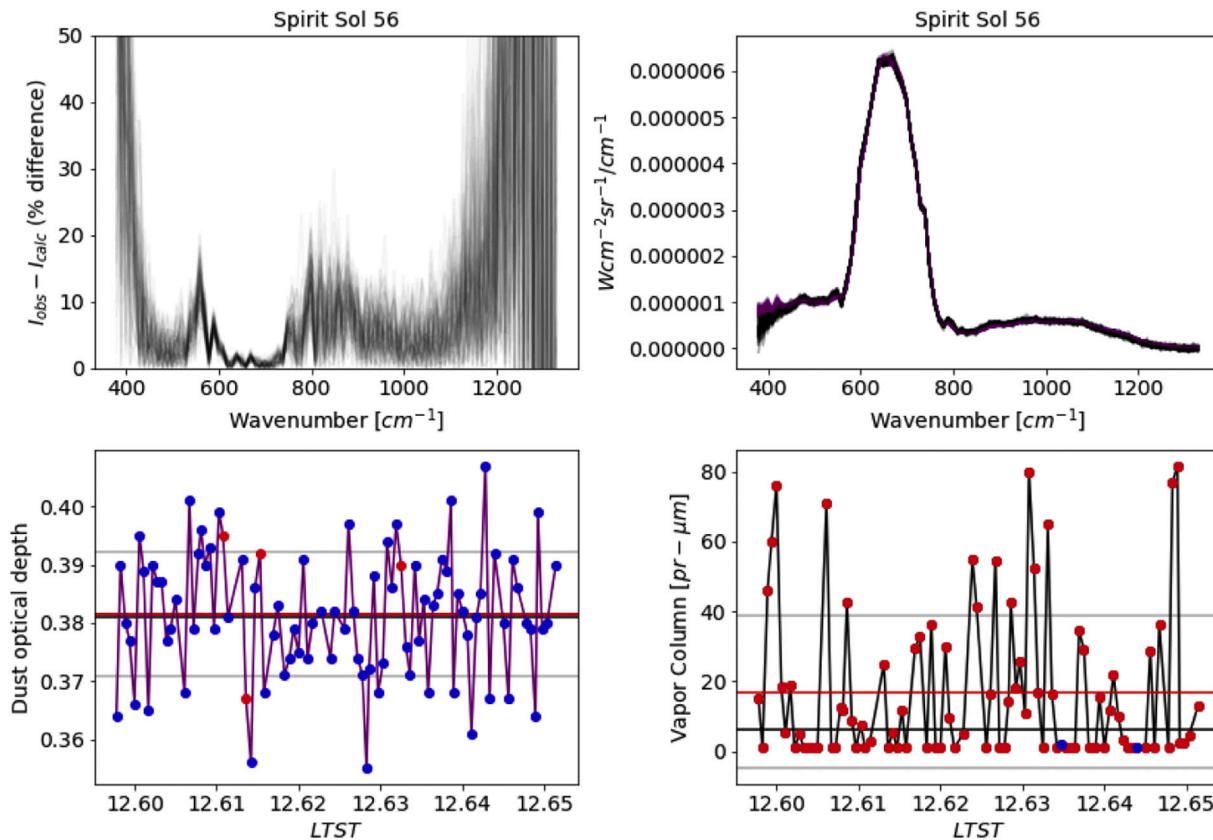

Fig. 2. (Top Left) The relative difference between best-fit model output and observational spectra for Spirit sol 56, (Top Right) and model/observation results. (Bottom Left) Dust optical depth retrieved on an ICK-by-ICK basis, with red markers indicating relative differences greater than 10%. (Bottom Right) Water vapor column values where red markers indicate relative differences greater than 10%.
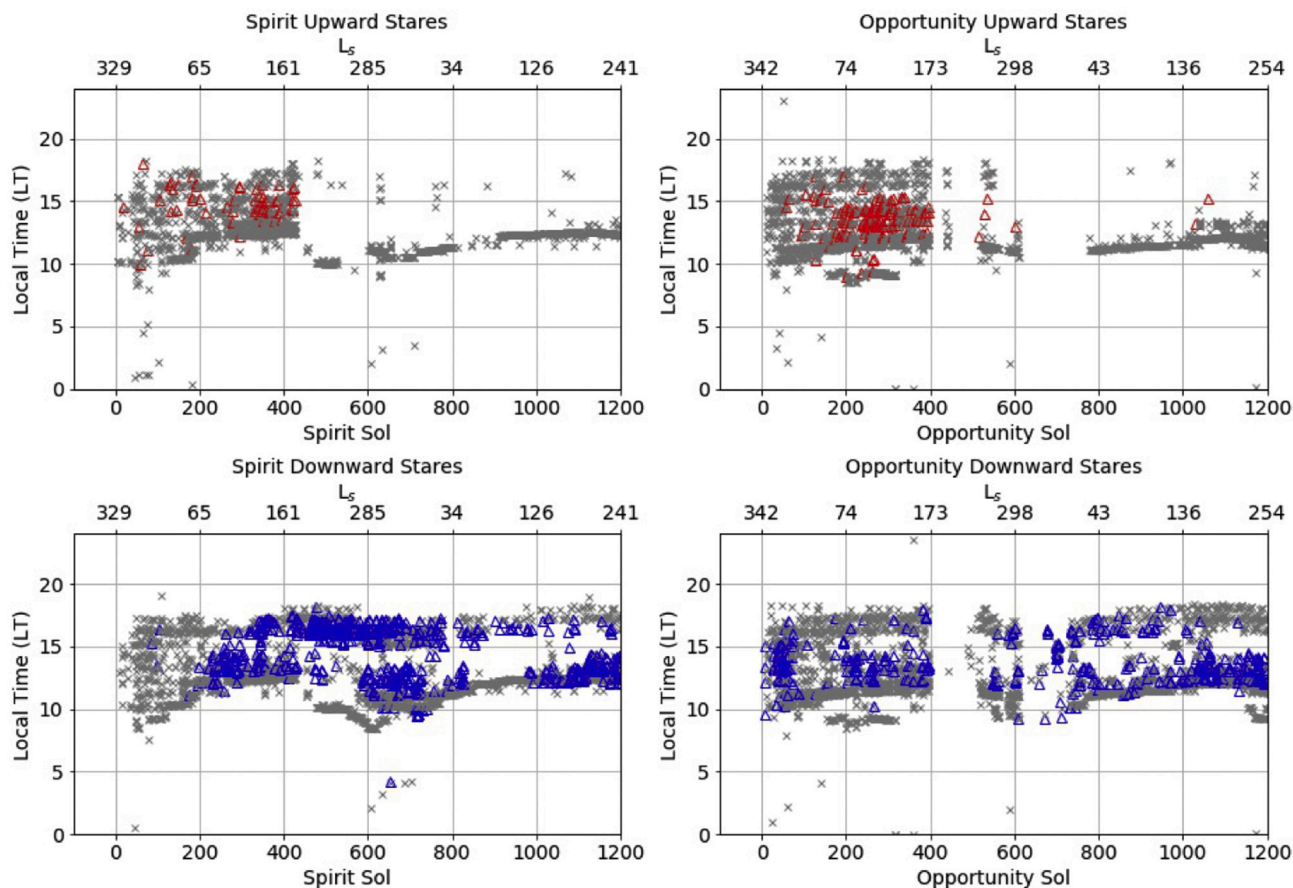
Fig. 3. Observations of Mini-TES atmospheric (top panels) and ground stares (bottom panels) for Spirit (left) and Opportunity (right). Red and blue triangles indicate long duration stares of approximately 30 min for upward-viewing stares and approximately 7 min for downward-viewing stares. (For interpretation of the references to colour in this figure legend, the reader is referred to the web version of this article.)

Fig. 1 shows an example of calibrated upward and downward-looking radiance spectra for Spirit, sol 102 (MY 27, $L_s = 20°$). The downward and upward-looking spectra are labeled as "ground" and "atmospheric" spectra, respectively. The spectral shape from downward-looking observations, or ground stares, follows that of a black-body curve except near 667 cm^{-1} (15 μm) where atmospheric CO_2 strongly absorbs. In contrast, upward-looking observations show a strong CO_2 emission feature at 15 μm. The resulting individually retrieved upward-looking temperature profiles for Spirit, sol 102, are shown on the right in Fig. 1. Variations in the colour of spectra and retrievals are representative of Local True Solar Time (LTST). For sol 102, five upward-looking observations were taken within the range of 02:00 LTST to 16:00 LTST. The resulting temperature profile structures (right panel, Fig. 1) are indicative of time of day. Early morning hours display an inversion layer close to the surface, while daytime profiles remain superadiabatic in the lowest 100 m above the surface well into late afternoon, as is discussed in Smith et al. (2006).

Dust and water vapor are retrieved separately in an iterative approach using upward-looking spectra for all ICKs in an observation. The retrieved dust optical depth is the normal-incidence column optical depth from the surface to infinity at 1075 cm^{-1} (9.3 μm). The column-abundance of water vapor is retrieved using the weak emission features observed between 380 cm^{-1} and 440 cm^{-1} (Smith et al. 2006). The formal uncertainty calculated from propagation of instrument noise is less than 1 K (Christensen et al. 2003; Smith et al. 2006). A conservative estimate for uncertainty in the accuracy of absolute temperature results is 2 K (Smith et al. 2006), which includes systematic uncertainties due to calibration and retrieval. However, spread in the ICK-by-ICK retrieval is in most cases less than the instrument noise. For this reason, we adopt a temperature uncertainty of 1 K.

Due to the nature of the retrieval, a damping parameter is included that controls how large changes in temperature can be within the algorithm. This parameter is tuned to be the least restrictive without introducing numerical instability and returning unphysical results (Smith et al. 1996). The resulting retrieval algorithm is robust, and systematic uncertainty within the retrieval is not expected to significantly affect the resulting perturbations within individual profiles.

Although the noise level in individual spectra does not significantly affect temperature retrievals, water vapor abundance cannot be reliably retrieved without averaging spectra. For example, using individual spectra obtained from the Spirit rover on sol 56, Fig. 2 top left panel shows the percent difference between each individual spectrum and its corresponding calculated spectrum following retrieval. Temperature retrievals performed using the individual spectra show good fits to the observed radiance. Within the range of 600 cm^{-1} to 750 cm^{-1}, the difference between the calculated and observed spectrum ($\Delta I/I_{obs}$ x 100) for each ICK within the observation is below 10%. Outside of this wavenumber range, percent difference increases. This is especially significant near the edges of the observational spectrum at 400 cm^{-1} where water vapor absorbs (Fig. 2, top left panel). Red markers in the bottom panels of Fig. 2 indicate individual retrievals where the relative difference between the calculated spectrum and observed spectrum is greater than 10%. This is shown for dust optical depth retrieval (left) and water vapor column abundance (right). Given the extremely low number of individually retrieved values for water vapor column abundance that produce fits to the model below a 10% difference, we choose not to analyze water vapor abundance using individual retrievals.
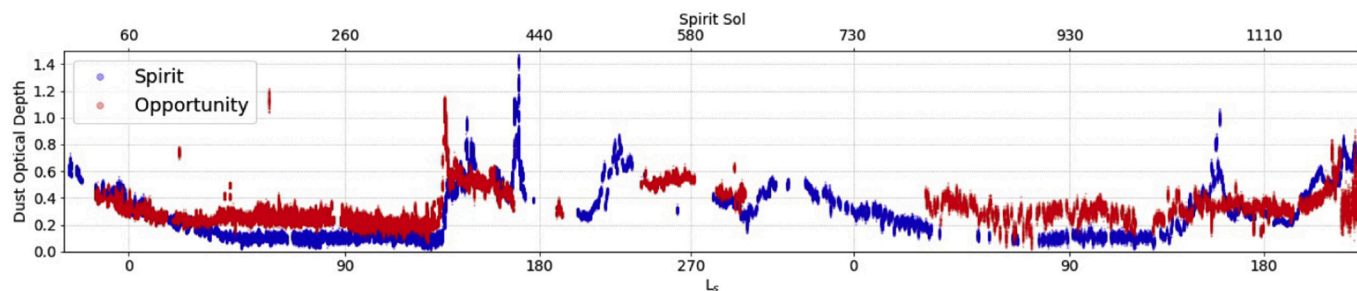
Fig. 4. Dust optical depth for Spirit (blue) and Opportunity (red) retrieved on an ICK-by-ICK basis. Results are plotted with respect to Spirit mission sols, when Spirit landed and began operations, with L_s values beginning in Mars Year 26 and ending in Mars Year 28. (For interpretation of the references to colour in this figure legend, the reader is referred to the web version of this article.)
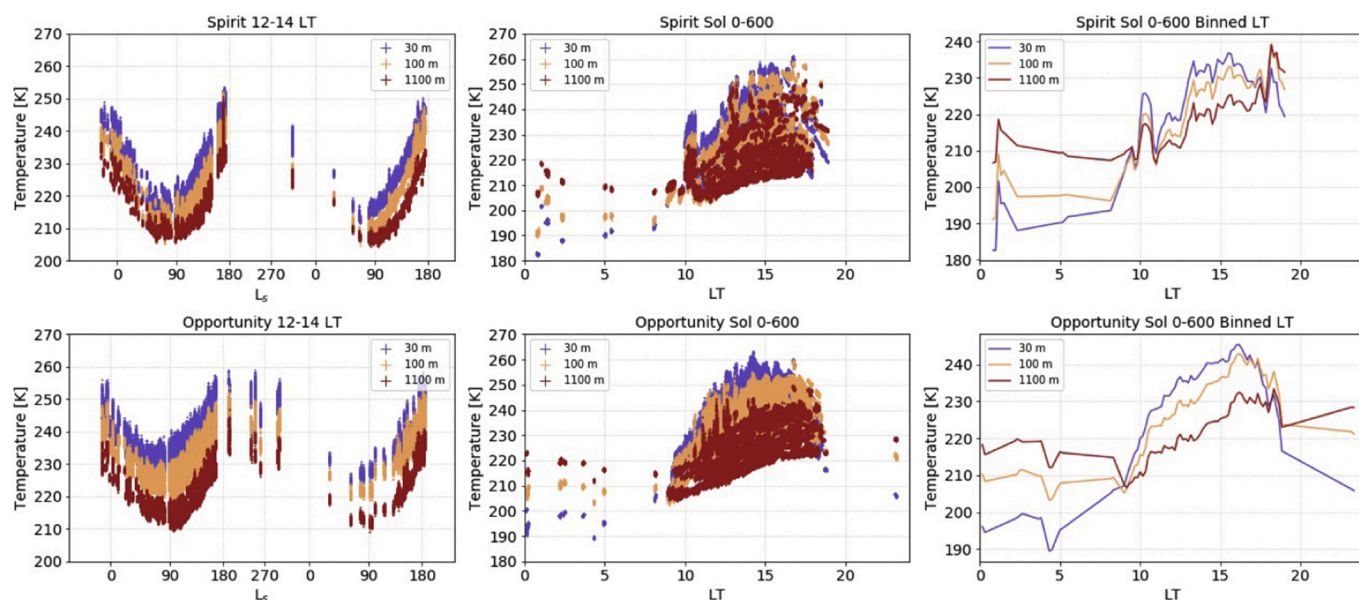

Fig. 5. Individual temperature retrieval results for Spirit (top panels) and Opportunity (bottom panels) as a function of season (left panels) and local time (middle panels). Seasonal variations are shown for observations between the local times of 12:00 and 14:00 LTST while diurnal variations are shown for sols 0–600. Additional diurnal behavior for sols 0–600 are shown as binned means every 10 min (right panels).

2.2. Availability

Individual spectra for Spirit and Opportunity have been processed in both the upward and downward-looking geometries up to sol 1200 (MY 28, $L_s = 241°$). Fig. 3 shows the distribution in sol number (season) and local time of upward and downward-looking stares, defined as observations taken at a single pointing elevation. The local times of stares mostly range from 10:00 LTST to 16:00 LTST for the first 400 sols for Spirit and Opportunity. Local time coverage is limited to late morning and noon hours following sol 600. Due to constraints on power usage overnight, early morning and late evening observations are infrequent. The few nighttime observations fall before sol 700. Long stares consisting of more than 900 spectra are denoted with red triangles.

Coverage for downward-viewing observations is more consistent across the dataset with local times ranging from 10:00 LTST to 18:00 LTST. This coverage extends fully to sol 1200 with a few minor gaps in data coverage due to operational constraints. The downward-looking observations in Fig. 3 represent both atmospheric and geologic observations. Long stares consisting of more than 200 spectra are denoted with blue triangles.

3. Results

3.1. Temperature and dust optical depth retrievals

The seasonal dependence of the individually retrieved dust optical depth shown in Fig. 4 follows the same pattern as the dust optical depth retrieved from direct imaging of the Sun by Pancam (Lemmon et al. 2015) as well as those retrieved up to 1.5 MY using full averaging (Smith et al. 2006). After sol 1200 of each mission, dust accumulation on the Mini-TES optics from the MY 28 global dust storm rendered the data unusable. The seasonal pattern is consistent with that observed from orbit (e.g., Smith et al., 2004), with higher dust optical depths recorded during the perihelion season ($L_s = 180°$–$360°$) and minimum values during the aphelion season ($L_s = 0°$–$180°$). There are no discernable diurnal patterns to the dust optical depth values retrieved by Mini-TES.

The rovers landed during the decay of a large regional dust storm, during which time Spirit recorded optical depths up to 0.6. Values reached minima near sols 200 and 900 ($L_s \sim 70°$ for MY 27 and 28) for both Spirit and Opportunity. Maximum dust optical depth for Spirit and Opportunity prior to the MY 28 global dust storm reached values of 1.4 and 1.2, respectively. These values occurred near Spirit sol 400 (MY 27, $L_s = 161°$), when dust activity increased near each rover (Lemmon et al. 2015).
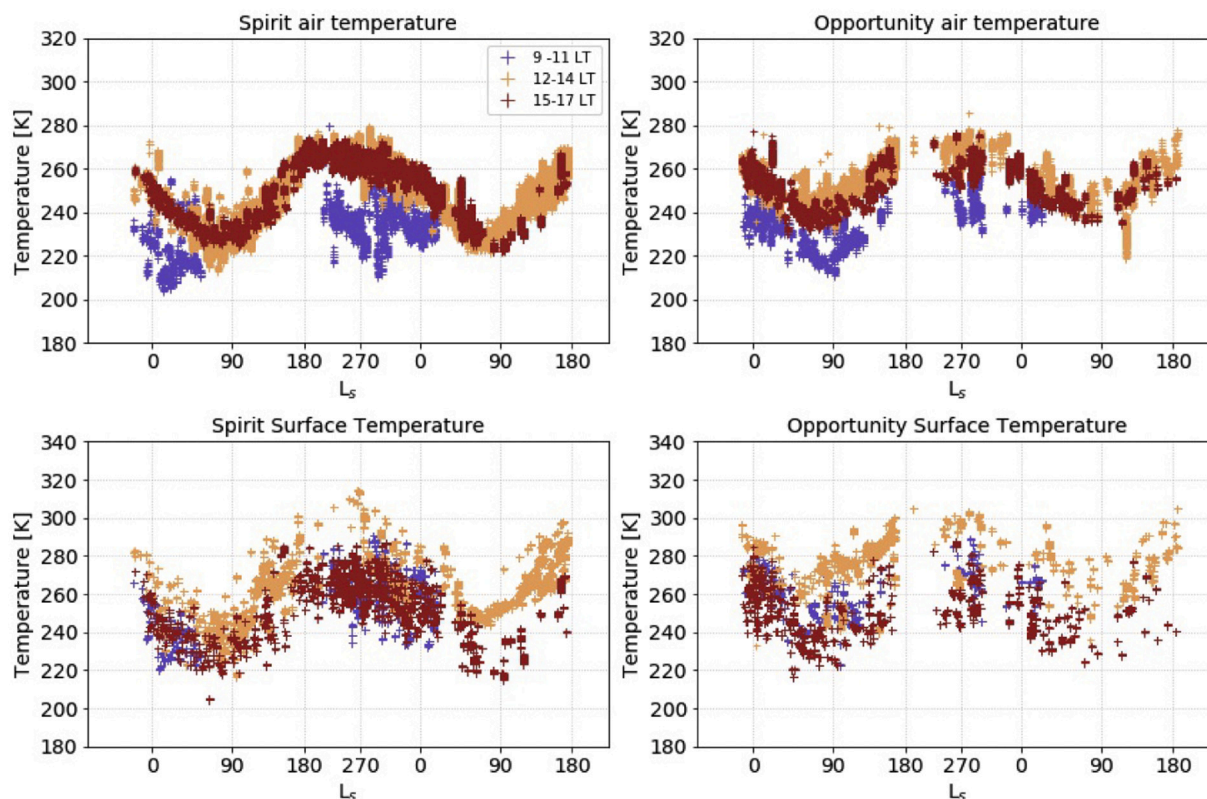
Fig. 6. Near-surface (top panel) and surface (bottom panel) temperature retrieval results for Spirit (left) and Opportunity (right). Air temperatures are representative of a height 1.1 m above the surface. Purple markers correspond to temperatures between 09:00 LTST and 11:00 LTST, orange markers correspond to temperatures between 12:00 LTST and 14:00 LTST, and red markers correspond to temperatures between 15:00 LTST and 17:00 LTST. (For interpretation of the references to colour in this figure legend, the reader is referred to the web version of this article.)

Fig. 5 shows the individual (ICK-by-ICK) temperature retrieval results for Opportunity (bottom panels) and Spirit (top panels). These results are an extension of those reported in Smith et al. (2006) but contain the ICK-by-ICK retrievals and extend past sol 600. The diurnal variations (middle and right panels) are shown for the first MY of operations (sols 1–600; MY 26, $L_s = 330°$ to MY 27, $L_s = 286°$), but the results shown in Fig. 5 are consistent with retrievals from the next MY as well. The seasonal variation of atmospheric temperatures shown in the top panels are given for retrievals during the local times of 12:00 LTST to 14:00 LTST, since observations are more frequent during those local times. Atmospheric temperatures between 12:00 and 14:00 LTST range between 200 K and 260 K for both rovers. Including other local times, the full range of temperatures for both rovers fall between 180 K and 270 K at a height of 30 m above the surface, while the temperatures at a height of 1000 m fall between 200 K and 250 K. The seasonal patterns for Spirit and Opportunity are similar, but atmospheric temperatures at the location of the Spirit rover are mostly lower than those from Opportunity due to the higher latitude of the Spirit site.

The right panels of Fig. 5 show the 10-min mean temperatures for the first 600 sols. For both rovers, diurnal temperatures display a distinct inversion over nighttime hours, where air temperature increases with increasing height above the surface. During the day, the diurnal variation of atmospheric temperatures differs between Opportunity and Spirit, with Spirit showing greater variability in temperatures between the hours of 12:00 and 18:00 LTST. However, the nighttime temperature inversion is present in the right panels Fig. 5 for all three heights above the surface for both rovers. This inversion begins between the hours of 15:00 and 19:00 LTST. For Spirit and Opportunity, the nighttime temperature inversion is still present well after sunrise (06:00 LTST). This inversion does not completely disappear until ~09:00 LTST when convective activity sharply increases. This is expected, as convection,

which drives fluctuations in temperature, is initiated from warming below.

The seasonal variation of near-surface atmospheric and surface temperatures retrieved from downward-viewing spectra are shown in Fig. 6. The results contain ICK-by-ICK retrievals, extended past sol 600 of the mission, and include dedicated geologic observations. These results are consistent with the fully-averaged results presented in Spanovich et al. (2006). Including morning observations, near-surface atmospheric temperatures at the Opportunity site fall within the range of 180 K to 280 K. Spirit near-surface atmospheric temperatures mainly fall within the range of 188 K to 280 K. The seasonal patterns between Spirit and Opportunity are similar, following the amount of solar insolation available at the surface.

Fig. 7 shows the diurnal variation in near-surface atmospheric and surface temperatures for three MY. The diurnal variation of atmospheric temperatures shown in the top panels of Fig. 7 peaks near 15:00 LTST for Spirit and 14:00 LTST for Opportunity in response to surface heating from below. Atmospheric temperatures are determined by the balance between radiative cooling and surface heating, causing a delay in the peak of near-surface atmospheric temperatures relative to surface temperatures. The diurnal pattern for both rovers follows a similar trend when compared to temperature measurements from other missions (Martínez et al. 2017) with morning temperatures between the hours 09:00 LTST and 11:00 LTST much lower than afternoon temperatures between the hours of 12:00 LTST and 17:00 LTST. Surface temperatures closely follow solar heating and are highest near noon, while air temperatures, which increase due to heating from surface emission, are highest near 15:00 LTST.

Spirit near-surface atmospheric temperatures show more variability, which is consistent with variable surface temperatures as the near-surface air is expected to respond to local changes in surface
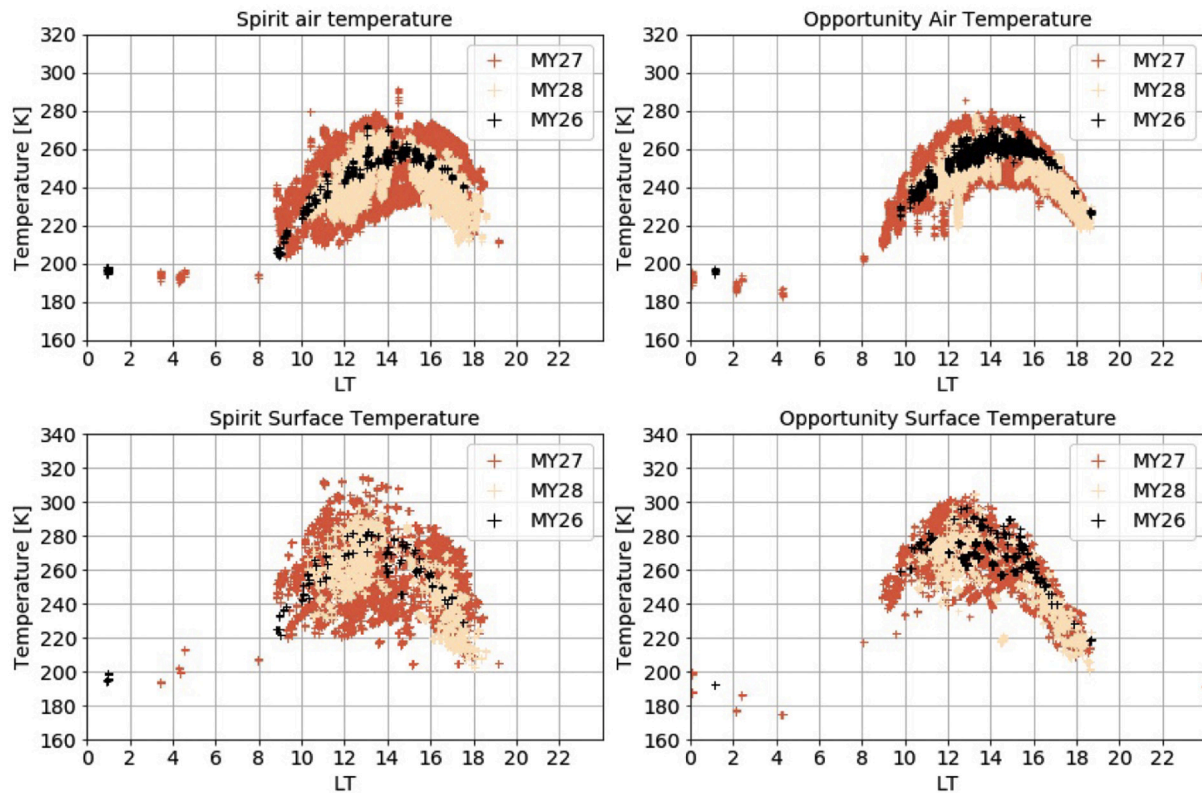
Fig. 7. Diurnal variation of near-surface atmospheric temperature (top panels) and surface temperature (bottom panels) retrievals for Spirit (left panels) and Opportunity (right panels).
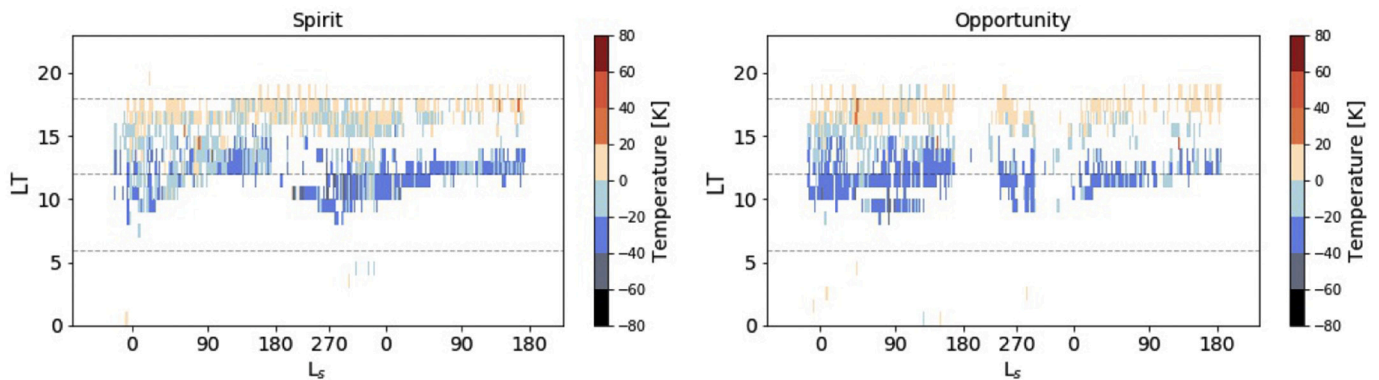

Fig. 8. Hourly mean differences between surface and near-surface atmospheric temperatures for Spirit (left panel) and Opportunity (right panel).

properties. Opportunity maximum diurnal surface temperatures can peak just over 300 K, and the minimum recorded for morning observations is near 175 K. The difference between the diurnal maximum and minimum surface temperatures is larger at Opportunity than at Spirit. Year-to-year variability in near-surface atmospheric and surface temperatures for MY 27 and 28 is relatively low for both rovers outside of the strongest dust storms. There is repeatability even during the dustier perihelion season. Despite having fewer observations for MY 26, there is a discernable diurnal pattern similar to that of MY 27 and 28.

While the two rovers show similar seasonal behavior, the diurnal surface temperature patterns between Spirit and Opportunity differ significantly. Opportunity shows a very well-defined diurnal pattern, with large differences between the minimum and maximum temperatures. Surface temperatures peak at noon for both rovers, fall off quickly after noon, and reach minimums between the hours of 04:00 LTST and 06:00 LTST. On the other hand, Spirit surface temperatures are much

more variable. This is consistent with previous work (Spanovich et al. 2006). There is no discernable seasonal pattern to surface temperature variability, and the variability is likely due to changes in the local surface properties. Surface temperature in part is affected by visible albedo and thermal inertia, and the terrain in Gusev Crater (Spirit rover site) is less homogeneous than at Meridiani Planum (Opportunity rover site) (e. g., Bell et al., 2004a,b; Christensen et al. 2004a, 2004b).

The temperature difference between the surface and atmosphere drives turbulent responses during the day. Fig. 8 shows the mean hourly surface-atmosphere temperature differences for Spirit (left) and Opportunity (right). Sunset (18:00 LTST), sunrise (06:00 LTST), and noon are marked by dotted horizontal lines. Near-surface atmospheric temperatures for both rovers are colder than the surface during daytime hours and become warmer than the surface after about 16:00 LTST when surface temperatures quickly drop due to a reduction in solar insolation as the Sun sets. The local time of this change is much more consistent at
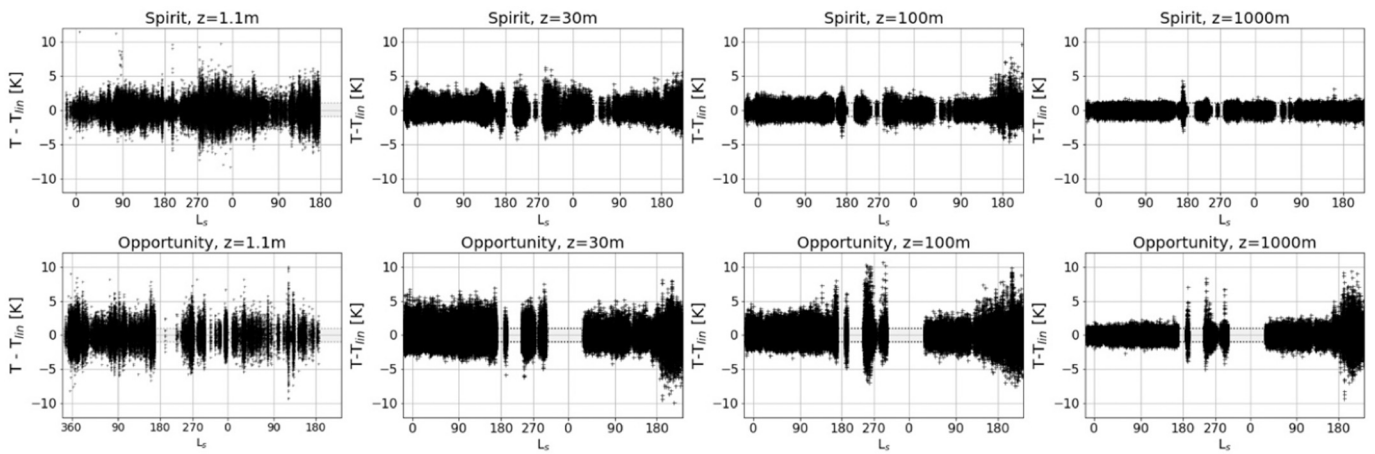
Fig. 9. Seasonal variation of detrended atmospheric temperature fluctuations for Spirit (top panels) and Opportunity (bottom panels) at four vertical levels above the surface.
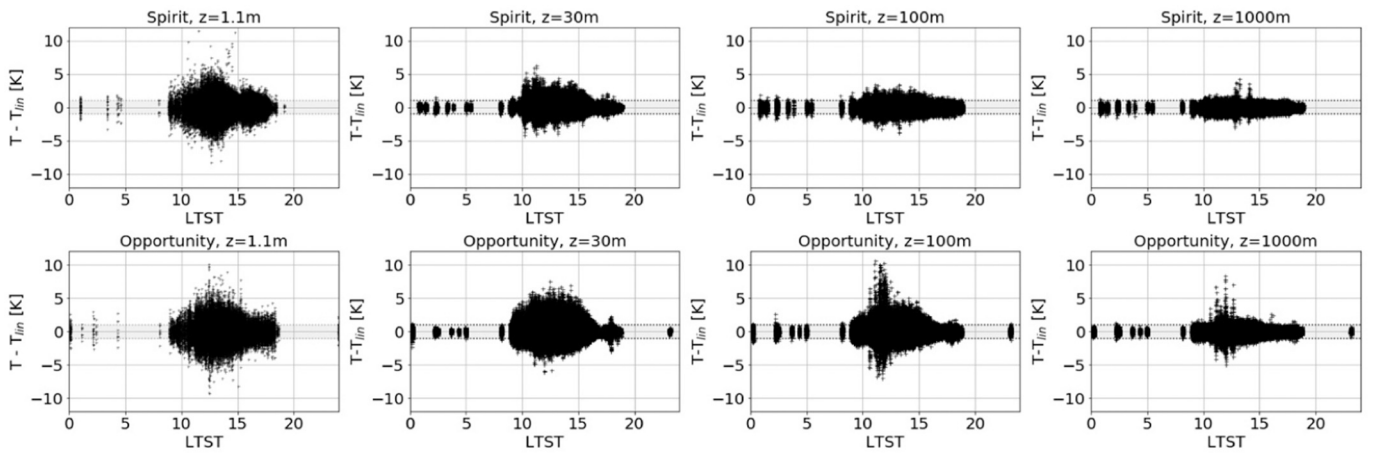

Fig. 10. Diurnal detrended atmospheric temperature fluctuations for Spirit (top panels) and Opportunity (bottom panels) at four heights above the surface.

Opportunity than at Spirit. Between the hours of 10:00 LTST and 12:00 LTST, the surface-atmosphere absolute temperature differences at Opportunity mostly fall between 20 and 40 K. This difference is reduced between the hours of 13:00 LTST and 15:00 LTST to 0 to 20 K. Spirit shows similar patterns after MY 27, $L_s = 286°$, where absolute

temperature differences between 20 and 40 K are achieved between 10:00 LTST and 13:00 LTST. Prior to this, the temperature difference is more variable.
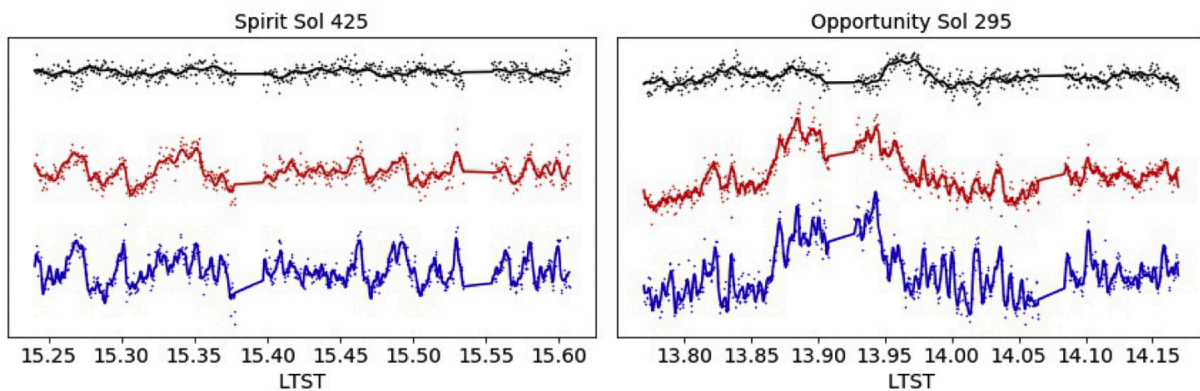

Fig. 11. Examples of temperature time series for Spirit and Opportunity at 30 m (blue or bottom curves), 100 m (red or middle curves), and 1000 m (black or top curves). Linearly detrended temperature data points are plotted as dots and the low pass filtered signal is plotted as a solid line. Temperature deviations for each height are offset to show the general shape and appearance of the fluctuations. Typical amplitude of the fluctuations at 30 m is between 1 and 2 K. (For interpretation of the references to colour in this figure legend, the reader is referred to the web version of this article.)
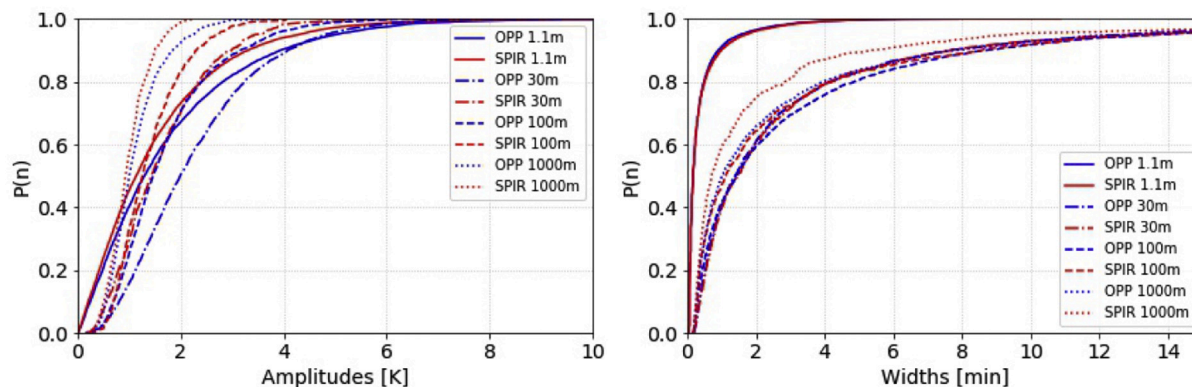
Fig. 12. Cumulative distribution functions of peak-to-peak amplitudes (left panel) and full width timescales in minutes (right panel) for Spirit and Opportunity at four vertical levels.

3.2. Temperature fluctuations

The ICK-by-ICK fluctuations in retrieved atmospheric temperatures provide information on atmospheric turbulence. For each Mini-TES observation, a linear trend is fit to the retrieved temperatures and is then subtracted from the observation to remove the effect of the diurnal temperature change. This detrending is completed for each observation at each height for upward stares. For downward stares, the surface temperature does not vary outside of ± 1 K, so only near-surface atmospheric temperature is detrended. Resulting temperature deviations are shown in Fig. 9 and Fig. 10. Results are shown up to the MY 28 global dust storm (sol 1200). The distribution of resulting deviations is skewed towards positive values. This skew decreases with increasing altitude, but holds up to 1 km. This is consistent with upwelling convective behavior (Tillman et al., 1972).

An example of the ICK-by-ICK detrended temperature retrievals is shown in Fig. 11. The resulting time series are non-periodic and stochastic but are embedded with regular patterns. The ICK-to-ICK noise level (~0.2 K) is much smaller than the estimated uncertainty in absolute temperature. The temperature fluctuations that are evident in the detrended signal are larger than the noise level and are real temperature changes over short timescales indicative of convective activity. These temperature fluctuations last anywhere from about 10 s to several minutes.

3.2.1. Seasonal variation of fluctuations

As shown in Fig. 9, near-surface atmospheric temperature fluctuations at a height of 1.1 m for Spirit are mostly between 1 and 7 K, with occasional fluctuations greater than 10 K. There is a seasonal trend to near-surface temperature fluctuations seen at the Spirit rover location, where minima occur when solar insolation is at a minimum ($L_s = 71°$, sols ~250 and ~ 925). The apparent minimum for Spirit near MY 27, L_s = 220° (sol 500), during the dusty season is not due to an actual minimum in the deviations but instead is a result of a lack of midday observations where the largest deviations regularly occur. Opportunity temperature fluctuation are larger in magnitude than those of Spirit above 30 m, but seasonal trends are less evident. At the surface, the fluctuation magnitude is similar for the two rovers.

The seasonal trend in temperature fluctuations is less noticeable in the retrievals at 30 m and 100 m than in the near-surface atmospheric temperature retrievals and is almost non-existent at 1000 m. For temperatures at 1000 m, only large spikes are present and are coincident with a large increase in dust optical depth that occurred shortly after MY 27, L_s = 160° (sol 400, see Fig. 4). This increase is also noticeable in the 100 m temperature results. Opportunity shows similar trends, with seasonal trends less noticeable at 30 m and 100 m than near the surface. For Opportunity, large changes in the amplitude of fluctuations are coincident with increases in dust optical depth and are noticeable as high as 1000 m.

Between sol 1000 and sol 1200 (MY 28, L_s ~ 125°–240°), increases in fluctuation amplitude can be seen in Spirit temperature data up to 100 m. This increase, which is not present at 1000 m, is especially apparent at 100 m. Changes in fluctuation magnitude at 1.1 and 30 m are within the normal range. Atmospheric temperatures are increasing during this season (see Fig. 5 and Fig. 6). Observations during this time are concentrated near noon, and fluctuations are indicative of peak midday activity. Increases in the amplitude of temperature fluctuations at Opportunity before sol 1200 are noticeable at 30 m, 100 m, and 1000 m, but an increase in near-surface fluctuations is not evident. Where Spirit shows no increase in fluctuation amplitude at 1000 m during this time, the increase at Opportunity is as large as those seen near sol 400 and sol 600 (MY 27, L_s ~ 160°–290°).

3.2.2. Diurnal variation of fluctuations

A defining characteristic of the boundary layer compared to the free atmosphere is that it undergoes diurnal changes due to solar forcing (Stull 1988). The absolute temperatures in Fig. 7 and Fig. 5 all show diurnal variations with clearly defined maxima and minima. The diurnal variation of absolute temperature is less pronounced at higher altitudes, especially for Spirit. Temperature fluctuations also exhibit a diurnal trend for both rovers. Fig. 10 shows the fluctuations as a function of LTST. The 1 K level is shaded to indicate the uncertainty we have adopted for our results (section 2.1). Results include those up to MY 28, L_s = 180° (sol 1100) to exclude fluctuations caused prior to the MY 28 global dust storm.

For both rovers, temperature fluctuations increase throughout the morning hours, reach a maximum near noon, and then come to an abrupt cessation between 16:00 and 17:00 LTST as solar insolation decreases. The large drop in the magnitude of temperature fluctuations is concurrent with the surface temperature becoming cooler than atmospheric temperatures. At this point, the atmospheric temperature vertical profile begins developing an inversion from the surface up. Increases in the magnitude of fluctuations after this point are evident at the 30 m height level for both Opportunity and Spirit, consistent with what is likely forced convection. Opportunity shows large deviations near noon at z = 100 m that are also evident at z = 1000 m. From Fig. 9, it is clear that these large increases are associated with perihelion and could be a result of forcing from larger dynamic systems.

4. Discussion

4.1. Time-series analysis

To characterize the fluctuations like those shown in Fig. 11, we calculate the peak-to-peak amplitudes of the positive increases in detrended retrieved temperatures for both downward and upward long
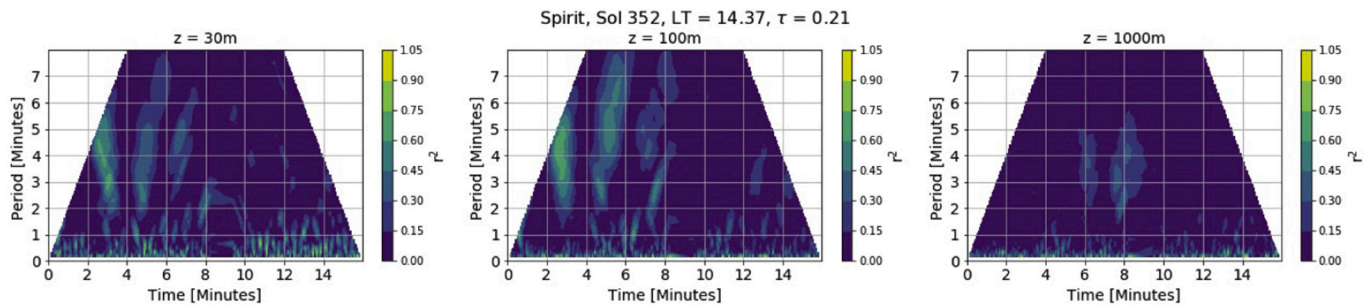
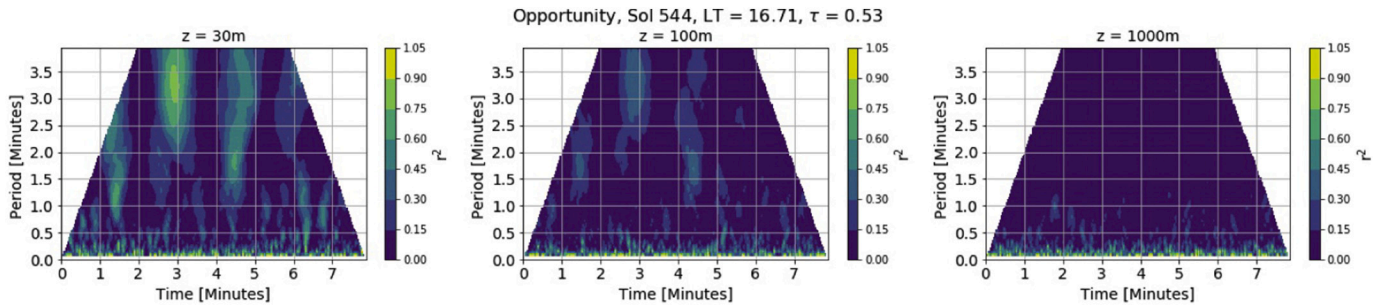**Fig. 13.** Spirit time series correlation example.

Fig. 14. Opportunity time series correlation example.

stares under the assumption that these increases are associated with turbulent structures. Long stares are defined as those lasting 30 min or more in upward-viewing mode and three minutes or more in downward-viewing mode. In addition, for each temperature fluctuation, we also calculate the width, or timescale, defined as the time difference between the minima that occur just before and after each fluctuation. For example, if the fluctuations are cosine in shape, then the peak-to-peak amplitude we compute would correspond to the full peak-to-peak amplitude of the cosine and the width would correspond to the full period of a wave.

The Cumulative Distribution Functions (CDF) of temperature fluctuation amplitudes (left panel) and widths (right panel) across all long stares are shown in Fig. 12. The CDF indicates the distribution of amplitudes and widths for a given atmospheric level. For example, the 100 m level at Spirit indicated by a dashed red line shows that 80% (P(n) = 0.8) of temperature fluctuations fall within an amplitude of 2 K. In this way, curves with steeper slopes contain fewer large-amplitude fluctuations. Spirit and Opportunity show similar patterns for amplitudes (left panel of Fig. 12), which decrease consistently with height for values derived from upward stares. For upward stares, fluctuation amplitudes

are larger for Opportunity than for Spirit at each atmospheric level. The CDF for near-surface amplitudes retrieved from downward-looking stares are plotted as solid lines. The larger slopes of both near-surface distributions indicate a relative lack of large amplitude fluctuations. However observation periods are shorter for downward-viewing stares compared to upward-viewing stares. Shorter observation periods mean that larger, longer structures are not captured in the temperature observations. The CDF for the full width timescales of the fluctuations are similar for Spirit and Opportunity and show less vertical variation than amplitudes.

In addition to calculating timescales and amplitudes, we also perform a frequency analysis. The signatures in the temperature time series are distinctly non-periodic, so we avoid the use of Fourier analysis, which assumes periodicity. Instead, for each ICK in a single observation, we calculate the correlation between the linearly detrended temperature and a cosine curve with a known period. We do this over a range of periods to determine the correlation of the signal to different timescales. The higher correlation values are associated with convective structures and provide insight into turbulent activity at each site. In this way, it is similar to a Fourier analysis. Figs. 13 and 14 show correlation values, r^2,
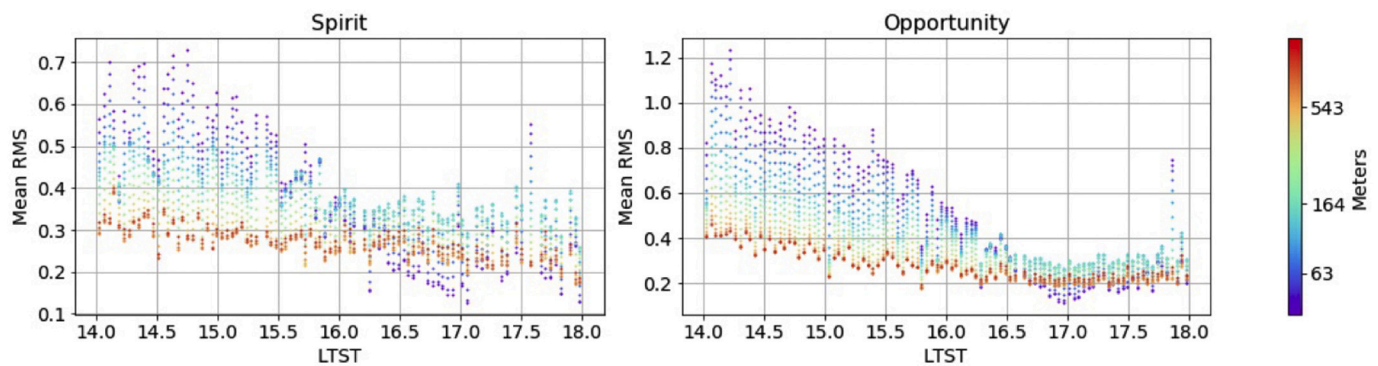

Fig. 15. Mean binned RMS amplitude of temperature fluctuations during late afternoon local times showing the distinctive quiet period near 17:00 LTST observed for both Spirit and Opportunity. The mean RMS amplitude of fluctuations decreases as a function of height for both rovers.
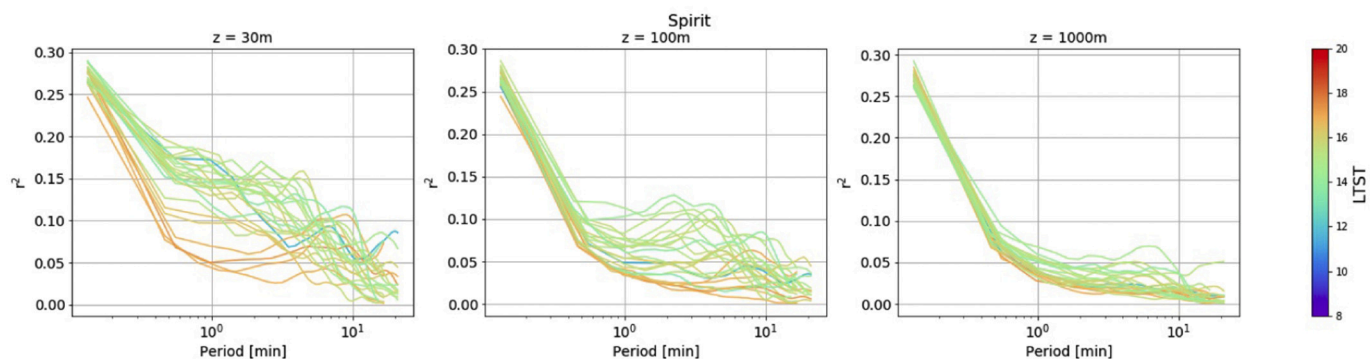
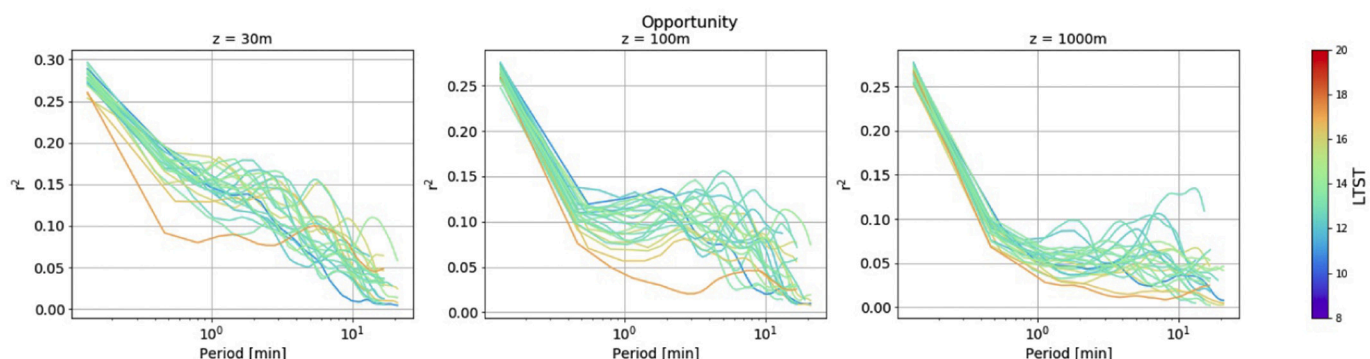**Fig. 16.** Averaged time series as a function of LTST for Spirit.

Fig. 17. Averaged time series correlation for Opportunity.

to different periods for each time step within an observation. For the Spirit observation shown in Fig. 13, there exist correlations with long-period fluctuations of a few minutes superimposed on short-period correlations that are present at every level. Long-period correlations are likely consistent with larger turbulent structures. These large structures are even more evident in Fig. 14 for Opportunity but decrease quickly with height.

4.2. Diurnal variations

While Mini-TES did not observe early morning hours as often as it observed afternoon hours, observations in the evening were frequent enough to capture the effects of surface forcing. Air-surface temperature differences consistently change sign from negative (atmosphere cooler than the surface) to positive (surface cooler than the atmosphere) between the hours of 15:00 LTST and 18:00 LTST for both Spirit and Opportunity. During this change in near-surface air and surface temperature difference, the observed temperature fluctuations decrease significantly.

Fig. 15 shows the binned, root mean square of temperature fluctuations at heights from 30 m (purple) up to 1000 m (red) above the surface. For Opportunity, the amplitude of temperature fluctuations systematically decreases at all heights, with a quiet period at 17:00 LTST for all sols. There is an increase in the fluctuations again near sunset when mechanical shear is expected to dominate turbulent behavior. The temperature fluctuations observed by Spirit show more variation, but the same decrease in activity is still evident in the late afternoon, and a quiet period near 17:00 LTST is visible for the lowest levels (purple).

We can also evaluate the amount of turbulent behavior for each observation longer than 10 min by averaging the time series correlations shown in Figs. 13 and 14 across local times in order to compare the variation of turbulent behavior for different periods. For this analysis, we calculated the mean r^2 value across a single observation for each

period. The results show which periods are more frequently correlated with large fluctuations. This was done for multiple observations to assess differences in local time and between the two rovers. Fig. 16 and Fig. 17 show that there are lower average values, which correspond to fewer convective events for observations near sunset (orange lines) than for daytime observations (green lines). This is more pronounced at lower heights and is likely a result of the change from free convection earlier during the afternoon to turbulent forcing from the surface during the evening. This decrease at sunset is a consistent atmospheric phenomenon that is observed at both rover sites across all seasons and in more recent work from InSight (Banfield et al. 2020).

4.3. Comparison of surface properties at each site

Convective activity is a response to radiative forcing from solar insolation, topography and large-scale atmospheric dynamics. The size of the response is dependent on surface properties such as thermal inertia and, to a lesser extent, albedo (Martínez et al. 2014). Thermal inertia is a metric for how much energy the surface can absorb without changing temperature. Surfaces with low thermal inertia tend to have large diurnal range in temperatures, whereas high thermal inertia surfaces have a smaller diurnal range of temperature.

Spirit and Opportunity landed in regions with distinct differences in terrain and surface properties. Within Gusev crater, the terrain encountered by the Spirit rover is a generally flat area where small rocks cover about 5% of the surface (Bell et al., 2004a). Optically thick coatings of fine-grained, bright dust cover most rocks and surfaces while exposed surfaces are darker (Bell et al., 2004a). Thermal inertia in Gusev Crater is highly variable, ranging from 150 to 450 J m^{-2} s$^{-0.5}$ K^{-1} (Christensen et al. 2004a). The Panoramic Camera (Pancam) calibrated broadband filter L1 739-nm estimates of albedo are 0.25, but the rover traversed through higher albedo regions up to 0.3 (Bell et al., 2004a).

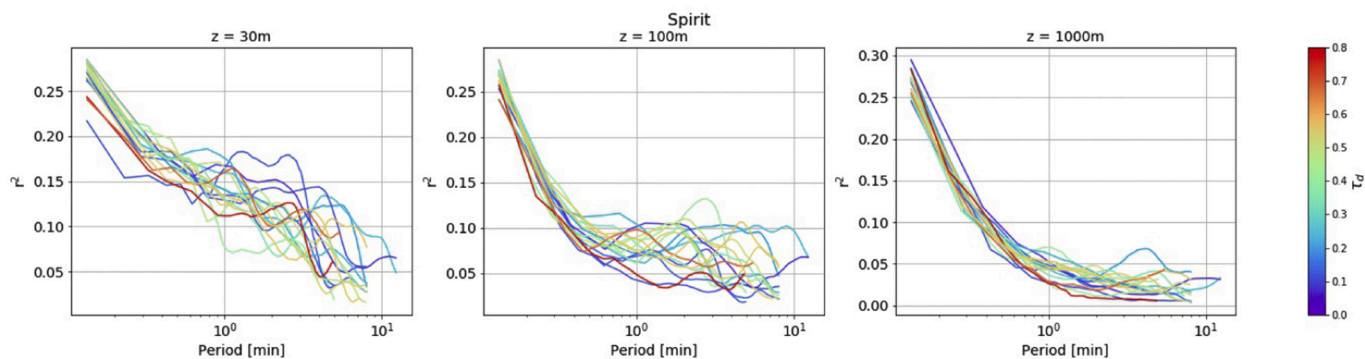Opportunity landed in a much darker region, dominated by dry,

Fig. 18. Spirit time-averaged correlations as a function of cosine period. The colors are indicative of optical depth.
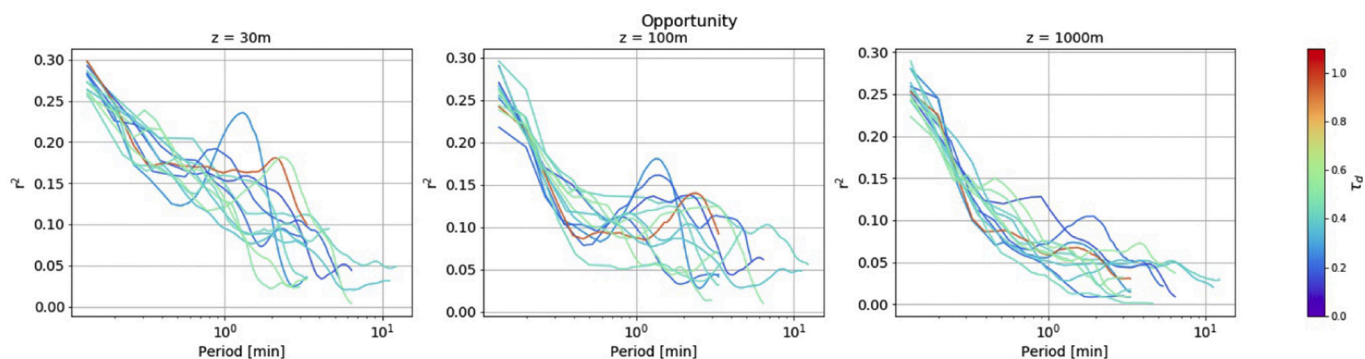

Fig. 19. Opportunity time-averaged correlations as a function of cosine period. The colors are indicative of optical depth.

loose, poorly sorted sand (Bell et al., 2004b). Pancam albedo estimates are 0.14 with some wind streaks as high as 0.25 (Bell et al., 2004b). The terrain was selected for its flat, safe topography (Squyres et al., 2004). Measurements from the THEMIS instrument on Mars Odyssey give a thermal inertia value for Meridiani Planum of 190 J m^{-2} s$^{-0.5}$ K^{-1} (Golombek et al. 2005) while the estimates from Mini-TES are closer to 100 J m^{-2} s$^{-0.5}$ K^{-1} (Fergason et al., 2006).

Surface temperatures retrieved from Spirit observations show a smaller difference between maximum and minimum values each sol, whereas Opportunity surface temperatures show a large diurnal temperature difference (Fig. 7). The near-surface atmospheric temperatures also show differences in their diurnal fluctuations between Spirit and Opportunity. The fluctuations seen in Gusev Crater (Spirit) are more indicative of varied terrain as opposed to fluctuations at Opportunity, which are less variable and indicative of a homogenous, darker surface with lower thermal inertia.

Recent work by Newman et al. (2019) has shown that surface-to-air temperature differences inside Gale Crater do not follow the thermal inertia patterns associated with the terrain and are instead dominated by topography. While topography in Meridiani Planum is mostly flat and homogeneous, Mini-TES measurements from Spirit were made in Gusev Crater. Within this crater, Spirit traversed over highly variable terrain as well as topography, arriving at Columbia Hills near sol 400 of the mission. While there is a topographical difference between Spirit and Opportunity, there is little discernable change to Spirit temperature fluctuations in Gusev Crater along the traverse path. This would suggest that the impact of topography at Spirit and Opportunity sites on temperature fluctuations is less than that of surface properties and solar heating.

4.4. Dust and turbulent behavior

Atmospheric temperature is linked to the dust cycle through radiative feedback. During the daytime, suspended dust tends to warm the atmosphere while cooling the surface (e.g., Smith 2004). Although we expect a large impact in the thermal state from dust lifting events at both rover sites, we observe no major changes in turbulent behavior for Mini-TES observations. Fig. 18 and Fig. 19 show the time-averaged correlation values for temperature fluctuations at Spirit and Opportunity, respectively. These correlation values are indicative of the rate of convective events with a given timescale (or period). The curves show fewer convective events (with large scatter) at longer periods and more convective events (higher correlation values) with short periods at all heights. The colors indicate optical depth and cover the timeframe of the first major increase in optical depth at Spirit and Opportunity near sol 350 (MY 26, L$_s$ ~ 135°).

The correlation values for times with high values of dust optical depth are not distinct from those with lower optical depth. While large-period fluctuations are present in some of the observations, there is no clear pattern associated with dust optical depth. The observed changes in correlation are more a function of height above the surface, with a higher number of longer-period fluctuations at lower heights. This is especially true for Spirit, which shows a considerable drop with height in the average correlation at longer periods for all optical depths.

While there is some evidence of increased fluctuation amplitudes with sudden increases in optical depth (see Fig. 9), these could also correspond to increased large-scale dynamics. Following increases in dust optical depth, cooling at the surface is observed to occur in the Mini-TES observations, but changes in the turbulent behavior, whether a decrease or increase, are not evident. The lack of a discernable response in convective activity with respect to optical depth is likely due to limited long duration coverage from Mini-TES observations and the relatively small amount of seasonal variation in the difference between surface temperatures and near-surface atmospheric temperatures, which can be a principal driver of convection.

5. Summary

The Mini-TES spectrometer carried by Spirit and Opportunity was a unique instrument that enabled vertical temperature profiles to be retrieved at high frequency (every 2 s). We have retrieved the ICK-by-ICK temperature profiles to characterize turbulent behavior at each rover site. In addition, we have retrieved ICK-by-ICK near-surface atmospheric and surface temperatures for a more complete view of the vertical and temporal variation of temperature fluctuations within the PBL.

There is a strong vertical variation in the amplitude and frequency of temperature fluctuations observed by both Spirit and Opportunity and there are large differences between their vertical structures. Although the diurnal variation in temperature fluctuations is almost non-existent for Spirit at 1000 m, a small diurnal variation in fluctuations is observed in observations from Opportunity at 1000 m, suggesting that the most active region of the boundary layer is deeper at Opportunity than at Spirit.

The high thermal inertia at the Spirit site is consistent with the observations that show a smaller diurnal temperature variation, shallower boundary layer height, and decreased turbulent activity at higher atmospheric levels observed by Mini-TES than at the Opportunity site. Temperature fluctuations are observed to be strongly controlled by the surface-air temperature difference, which varies little as a function of season at both rover sites. Fluctuations are observed to quickly diminish in the late afternoon reaching a minimum near 17:00 LTST followed by moderately increased activity near sunset caused by forced convection. There is no significant change in the observed convective activity as a function of dust optical depth during regional dust storms. The few large temperature fluctuations that are concurrent with dust events are likely the result of large-scale systems.

Declaration of Competing Interest

None.

References

Banerdt, W. Bruce, Smrekar, Suzanne E., Banfield, Don, Giardini, Domenico, Golombek, Matthew, Johnson, Catherine L., Lognonné, Philippe, Spiga, Aymeric, Spohn, Tilman, Perrin, Clément, Stähler, Simon C., Antonangeli, Daniele, Asmar, Sami, Beghein, Caroline, Bowles, Neil, Bozdag, Ebru, Chi, Peter, Christensen, Ulrich, Clinton, John, Collins, Gareth S., Daubar, Ingrid, Dehant, Véronique, Drilleau, Mélanie, Fillingim, Matthew, Folkner, William, Garcia, Raphaël F., Garvin, Jim, Grant, John, Grott, Matthias, Grygorczuk, Jerzy, Hudson, Troy, Irving, Jessica C.E., Kargl, Günter, Kawamura, Taichi, Kedar, Sharon, King, Scott, Knapmeyer-Endrun, Brigitte, Knapmeyer, Martin, Lemmon, Mark, Lorenz, Ralph, Maki, Justin N., Margerin, Ludovic, McLennan, Scott M., Michaut, Chloe, Mimoun, David, Mittelholz, Anna, Mocquet, Antoine, Morgan, Paul, Mueller, Nils T., Murdoch, Naomi, Nagihara, Seiichi, Newman, Claire, Nimmo, Francis, Panning, Mark, Pike, W. Thomas, Plesa, Ana-Catalina, Rodriguez, Sébastien, Rodriguez-Manfredi, Jose Antonio, Russell, Christopher T., Schmerr, Nicholas, Siegler, Matt, Stanley, Sabine, Stutzmann, Eléanore, Teanby, Nicholas, Tromp, Jeroen, van Driel, Martin, Warner, Nicholas, Weber, Renee, Wieczorek, Mark, 2020. Initial results from the InSight mission on Mars. Nat. Geosci. 13, 183–189.

Banfield, D., Spiga, A., Newman, C., Forget, F., Lemmon, M., Lorenz, R., Murdoch, N., Viudez-Moreiras, D., Pla-Garcia, J., Garcia, R.F., Lognonné, P., 2020. The atmosphere of Mars as observed by InSight. Nature Geoscience 1–9.

Bell III, J.F., Squyres, S.W., Arvidson, R.E., Arneson, H.M., Bass, D., Blaney, D., Cabrol, N., Calvin, W., Farmer, J., Farrand, W.H., Goetz, W., Golombek, M., Grant, J. A., Greeley, R., Guinness, E., Hayes, A.G., Hubbard, M.Y.H., Herkenhoff, K.E., Johnson, M.J., Johnson, J.R., Joseph, J., Kinch, K.M., Lemmon, M.T., Li, R., Madsen, M.B., Maki, J.N., Malin, M., McCartney, E., McLennan, S., McSween Jr., H. Y., Ming, D.W., Moersch, J.E., Morris, R.V., Noe Dobrea, E.Z., Parker, T.J., Proton, J., Rice Jr., J.W., Seelos, F., Soderblom, J., Soderblom, L.A., Sohl-Dickstein, J.N., Sullivan, R.J., Wolff, M.J., Wang, A., 2004a. Pancam multispectral imaging results from the Spirit rover at Gusev crater. Science 305.

Bell III, J.F., Squyres, S.W., Arvidson, R.E., Arneson, H.M., Bass, D., Calvin, W., Farrand, W.H., Goetz, W., Golombek, M., Greeley, R., Grotzinger, J., Guinness, E., Hayes, A.G., Hubbard, M.Y.H., Herkenhoff, K.E., Johnson, M.J., Johnson, J.R., Joseph, J., Kinch, K.M., Lemmon, M.T., Li, R., Madsen, M.B., Maki, J.N., Malin, M., McCartney, E., McLennan, S., McSween Jr., H.Y., Ming, D.W., Morris, R.V., Noe Dobrea, E.Z., Parker, T.J., Proton, J., Rice Jr., J.W., Seelos, F., Soderblom, J.M., Soderblom, L.A., Sohl-Dickstein, J.N., Sullivan, R.J., Weitz, C.M., Wolff, M.J., 2004b. Pancam multispectral imaging results from the opportunity rover at Meridiani Planum. Science 306.

Christensen, Philip R., Mehall, Greg L., Silverman, Steven H., Anwar, Saadat, Cannon, George, Gorelick, Noel, Kheen, Rolph, Tourville, Tom, Bates, Duane, Ferry, Steven, Fortuna, Teresa, Jeffryes, John, O'Donnell, William, Peralta, Richard, Wolverton, Thomas, Blaney, Diana, Denise, Robert, Rademacher, Joel, Morris, Richard V., Squyres, Steven, 2003. Miniature thermal emission spectrometer for the Mars exploration rovers. Jour. Geophys. Res. 108 (E12), 8064. https://doi.org/10.1029/2003JE002117.

Christensen, P.R., Ruff, S.W., Fergason, R.L., Knudson, A.T., Anwar, S., Arvidson, R.E., Bandfield, J.L., Blaney, D.L., Budney, C., Calvin, W.M., Glotch, T.D., Golombek, M. P., Gorelick, N., Graff, T.G., Hamilton, V.E., Hayes, A., Johnson, J.R., McSween Jr., H.Y., Mehall, G.L., Mehall, L.K., Moersch, J.E., Morris, R.V., Rogers, A. D., Smith, M.D., Squyres, S.W., Wolff, M.J., Wyatt, M.B., 2004a. Initial results from the mini-TES experiment in Gusev crater from the Spirit rover. Science 305 (5685), 837–842. https://doi.org/10.1126/science.1100564.

Christensen, P.R., Wyatt, M.B., Glotch, T.D., Rogers, A.D., Anwar, S., Arvidson, R.E., Bandfield, J.L., Blaney, D.L., Budney, C., Calvin, W.M., Fallacaro, A., Fergason, R.L., Gorelick, N., Graff, T.G., Hamilton, V.E., Hayes, A.G., Johnson, J.R., Knudson, A.T., McSween Jr., H.Y., Mehall, G.L., Mehall, L.K., Moersch, J.E., Morris, R.V., Smith, M. D., Squyres, S.W., Ruff, S.W., Wolff, M.J., 2004b. Mineralogy at Meridiani Planum from the mini-TES experiment on the opportunity rover. Science 306 (5702), 1733–1739. https://doi.org/10.1126/science.1104909.

Davy, R.D., Davis, J.A., Taylor, P.A., 2010. Initial analysis of air temperature and related data from the Phoenix MET station and their use in estimating turbulent heat fluxes. J. Geophys. Res 115 (E3). https://doi.org/10.1029/2009JE003444.

Fergason, Robin L., Christensen, Philip R., Bell III, James F., Golombek, Matthew P., Herkenhoff, Kenneth E., Kieffer, Hugh H., 2006. Physical properties of the Mars Exploration Rover landing sites as inferred from Mini-TES—derived thermal inertia. Jour. Geophys. Res 111. https://doi.org/10.1029/2005JE002583. E02S21.

Golombek, M.P., Arvidson, R.E., Bell III, J.F., Christensen, P.R., Crisp, J.A., Crumpler, L. S., Ehlmann, B.L., Fergason, R.L., Grant, J.A., Greeley, R., Haldermann, A.F.C., Kass, D.M., Parker, T.J., Schofield, J.T., Squyres, S.W., Zurek, W., 2005. Assessment of Mars exploration rover landing site predictions. Nature 436, 44–48. https://doi.org/10.1038/nature03600.

Gómez-Elvira, J., Armiens, C., Castaner, L., Dominguez, M., Genzer, M., Gomez, F., Haberle, R., Harri, A.-M., Jimenez, V., Kahanpaa, H., Kowalski, L., Lepinette, A., Martin, J., Martinez-Frias, J., Mcewan, I., Mora, L., Moreno, J., Navarro, S., De Pablo, M.A., Peinado, V., Pena, A., Polkko, J., Ramos, M., Renno, N.O., Ricart, J., Richardson, M., Rodriguez-Manfredi, J., Romeral, J., Sebastian, E., Serrano, J., de la Torre Juarez, M., Torres, J., Torrero, F., Urqui, R., Vazquez, L., Velasco, T., Verdasca, J., Zorzano, M.-P., Martin-Torres, J., 2012. REMS: The Environmental Sensor Suite for the Mars Science Laboratory Rover. Space Sci. Rev. https://doi.org/10.1007/s11214-012-9921-1.

Grotzinger, John P., Crisp, Joy, Vasavada, Ashwin R., Anderson, Robert C., Baker, Charles J., Barry, Robert, Blake, David F., Conrad, Pamela, Edgett, Kenneth S., Ferdowski, Bobak, Gellert, Ralf, Gilbert, John B., Golombek, Matt, Gómez-Elvira, Javier, Hassler, Donald M., Jandura, Louise, Litvak, Maxim, Mahaffy, Paul, Maki, Justin, Meyer, Michael, Malin, Michael C., Mitrofanov, Igor, Simmonds, John J., Vaniman, David, Welch, Richard V., Wiens, Roger C., 2012. Mars Science Laboratory Mission and Science Investigation. Space Science Review 170, 5–56. https://doi.org/10.1007/s11214-012-9892-2.

Gunnlaugsson, H.P., Holstein-Rathlou, C., Merrison, J.P., Knak Jensen, S., Lange, C.F., Larsen, S.E., Madsen, M.B., Nørnberg, P., Bechtold, H., Hald, E., Iversen, J.J., Lange, P., Lykkegaard, F., Rander, F., Lemmon, M., Renno, N., Taylor, P., Smith, P., 2008. Telltale wind indicator for the Mars Phoenix lander. J. Geophys. Res 113. https://doi.org/10.1029/2007JE003008. E00A04.

Hess, S.L., Henry, R.M., Leovy, C.B., Ryan, J.A., Tillman, J.E., 1977. Meteorological results from the surface of Mars: Viking 1 and 2. Jour. Geophys. Res. 82 (28), 4559–4574.

Lacis, Andrew A., Oinas, Valdar, 1991. A description of the correlated k distribution method for modeling nongray gaseous absorption, thermal emission, and multiple scattering in vertically inhomogeneous atmospheres. Jour. Geophys. Res. 96 (D5), 9027–9063.

Larsen, S.E., Jørgensen, H.E., Landberg, L., et al., 2002. Aspects of the atmospheric surface layers on Mars and earth. Bound.-Layer Meteorol. 105, 451–470. https://doi.org/10.1023/A:1020338016753.

Lemmon, Mark T., Wolff, Michael J., Bell, James F., Smith, Michael D., Cantor, Bruce A., Smith, Peter H., 2015. Dust aerosol, clouds, and the atmospheric optical depth record over 5 Mars years of the Mars exploration rover mission. Icarus 251, 96–111. https://doi.org/10.1016/j.icarus.2014.03.029.

Martínez, Germán, Valero, Francisco, Vázquez, Luis, 2009. Characterization of the Martian convective boundary layer. Journal of the atmospheric science 66 (7), 2044–2058.

Martínez, G.M., Rennó, N., Fischer, E., Borlina, C.S., Hallet, B., de la Torre Juárez, M., Vasavada, A.R., Ramos, M., Hamilton, V., Gomez-Elvira, J., Haberle, R.M., 2014.

Surface energy budget and thermal inertia at Gale crater: calculations from ground-based measurements. Journal of Geophysical Research: Planets 119, 1822–1838. https://doi.org/10.1002/2014JE004618.

Martínez, G.M., Newman, C.N., De Vicente-Retortillo, A., Fischer, E., Renno, N.O., Richardson, M.I., Fairén, A.G., Genzer, M., Guzewich, S.D., Haberle, R.M., Harri, A.-M., Kemppinen, O., Lemmon, M.T., Smith, M.D., de la Torre-Juárez, M., Vasavada, A. R., 2017. The modern near-surface Martian climate: a review of in-situ meteorological data from Viking to curiosity. Space Sci. Rev. 212, 295–338. https://doi.org/10.1007/s11214-017-0360-x.

Miller, N., de la Torre Juárez, M., Tamppari, L., 2018. The effect of Bagnold dune slopes on the short timescale air temperature fluctuations at Gale crater on Mars. Geophys. Res. Lett. 45 (21), 11588–11594. https://doi.org/10.1029/2018GL080542.

Newman, C.E., Gómez-Elvira, J., Marin, M., Navarro, S., Torres, J., Richardson, M.I., Battalio, J.M., Guzewich, S.D., Sullivan, R., de la Torre, M., Vasavada, A.R., Bridges, N.T., 2017. Winds measured by the rover environmental monitoring station (REMS) during the Mars science laboratory (MSL) rover's Bagnold dunes campaign and comparison with numerical modeling using MarsWRF. Icarus 291, 203–231. https://doi.org/10.1016/j.icarus.2016.12.016.

Newman, C.E., Kahanpää, H., Richardson, M.I., Martínez, G.M., Vicente-Retortillo, A., Lemmon, M.T., 2019. MarsWRF Convective Vortex and Dust Devil Predictions for Gale Crater Over 3 Mars Years and Comparison With MSL-REMS Observations. Journal of Geophysical Research: Planets 124, 3442–3468. https://doi.org/10.1029/2019JE006082.

Read, P.B. Galperin, Larsen, S., Lewis, S., Mattanen, A., Petrosyan, A., Renno, N., Savijarvi, H., Sili, T., Spiga, A., Toigo, A., Vázquez, L., 2017. The Martian Planetary Boundary Layer. In: Haberle, R., Clancy, R., Forget, F., Smith, M., Zurek, R. (Eds.), *The Atmosphere and Climate of Mars* (Cambridge Planetary *Science*, pp. 172–202). Cambridge University Press, Cambridge. https://doi.org/10.1017/9781139060172.007.

Savijarvi, Hannu, 2012a. The convective boundary layer on Mars: Some 1-D simulation results. Icarus, Vol 221, 617–623. https://doi.org/10.1016/j.icarus.2012.08.016.

Savijarvi, Hannu, 2012b. Mechanisms of the diurnal cycle in the atmospheric boundary layer of Mars. Q. J. R. Meteorol. Soc., Vol 138, 552–560. https://doi.org/10.1002/qj.930.

Schofield, J.T., Barnes, J.R., Crisp, D., Haberle, R.M., Larsen, S., Magalhaes, J.A., Murphy, J.R., Seiff, A., Wilson, G., 1997. The Mars pathfinder atmospheric structure investigation/meteorology (ASI/MET) experiment. Science 278 (5344), 1752–1758. https://doi.org/10.1126/science.278.5344.1752.

Smith, M.D., 2004. Interannual variability in TES atmospheric observations of Mars during 1999-2003. Icarus 167, 148–165.

Smith, Micahel D., Barney J. Conrath, John C. Pearl, Eugene A Ustinov (1996). Retrieval of atmospheric temperatures in the Martian planetary boundary layer using upward-looking infrared spectra, Icarus, 124, 586–597.

Smith, Michael D., Wolff, Michael J., Lemmon, Mark T., Spanovich, Nicole, Banfield, Don, Budney, Charles J., Clancy, R. Todd, Ghosh, Amitabha,

Landis, Geoffrey A., Smith, Peter, Whitney, Barbara, Christensen, Philip R., Squyres, Steven W., 2004. First Atmospheric Science Results from the Mars Exploration Rovers Mini-TES. Science 306, 1750–1753. https://doi.org/10.1126/science.1104257.

Smith, M.D., Wolff, M.J., Spanovich, N., Ghosh, A., Banfield, D., Christensen, P.R., Landis, G.A., Squyres, S.W., 2006. One Martian year of atmospheric observations using MER Mini-TES. J. Geophys. Res 111, E12S13. https://doi.org/10.1029/2006JE002770.

Sorbjan, Zbigniew, Wolff, Michael, Smith, Michael D., 2009. Thermal structure of the atmospheric boundary layer on Mars based on mini-TES observations. Q. J. R. Meteorol. Soc 135, 1776–1787. https://doi.org/10.1002/qj.510.

Spanovich, N., Smith, M.D., Smith, P., Wolff, M.J., Christensen, P.R., Squyres, S.W., 2006. Surface and near-surface atmospheric temperatures for the Mars exploration rover landing sites. Icarus 180 (2), 314–320. https://doi.org/10.1016/j.icarus.2005.09.014.

Stull, R.B., 1988. An Introduction to Boundary Layer Meteorology. Springer.

Sutton, Jordan L., Leovy, Conway B., Tillman, James E., 1978. Diurnal variations of the Martian surface layer Metoeorological parameters during the first 45 sols at two Viking Lander sites. Jour. Atmos. Sci 35, 2346–2355.

Squyres, Steven W., Arvidson, Raymond E., Baumgartner, Eric T., Bell III, James F., Christensen, Philip R., Gorevan, Stephen, Herkenhoff, Kenneth E., Klingelhofer, Gostar, Madsen, Morten Bo, Morris, Richard V., Rieder, Rudolf, Romero, Raul A., 2003. Athena Mars rover science investigation. *J. Geophys. Res.*, Vol 108 (E12), 8062. https://doi.org/10.1029/2003JE002121.

Squyres, S.W., Arvidson, R.E., Bell III, J.F., Bruckner, J., Cabrol, N.A., Calvin, W., Carr, M.H., Christensen, P.R., Clark, B.C., Crumpler, L., Marais, D.J. Des, d'Uston, C., Economou, T., Farmer, J., Farrand, W., Folkner, W., Golombek, M., Gorevan, S., Grant, J.A., Greeley, R., Grotzinger, J., Haskin, L., Herkenhoff, K.E., Hviid, S., Johnson, J., Klingelhofer, G., Knoll, A.H., Landis, G., Lemmon, M., Li, R., Madsen, M. B., Malin, M.C., McLennan, S.M., McSween, H.Y., Ming, D.W., Moersch, J., Morris, R. V., Parker, T., Rice Jr., J.W., Richter, L., Rieder, R., Sims, M., Smith, M., Smith, P., Soderblom, L.A., Sullivan, R., Wanke, H., Wdowiak, T., Wolff, M., Yen, A., 2004. The Opportunity Rover's Athena Science Investigation at Meridiani Planum. Mars, Science 306 (5702), 1698–1703. https://doi.org/10.1126/science.1106171.

Taylor, Peter A., Catling, David C., Daly, Mike, Dickinson, Cameron S., Gunnlaugsson, Haraldur P., Harri, Ari-Matii, Lange, Carlos F., 2008. Temperature, pressure, and wind instrumentation in the Phoenix meteorological package. Jour. Geophys. Res 113, E00A10. https://doi.org/10.1029/2007/JE003015.

Tillman, J.E., 1972. Indirect determination of stability, heat and momentum fluxes in the atmospheric boundary layer from simple scalar variables during dry unstable conditions. Jour. App. Met. 11, 783–792.

Tillman, James E., Landberg, Lars, Larsen, Soren E., 1994. The boundary layer of Mars: fluxes, stability, turbulent spectra, and growth of the mixed layer. Amer. Met. Soc. 51 (12), 1709–1727.